Correcting for mantle dynamics reconciles Mid-Pliocene sea-level estimates

Fred D. Richards*[,1], Sophie L. Coulson[2], Mark J. Hoggard[3], Jacqueline Austermann[4], Blake Dyer[5], & Jerry X. Mitrovica[6]

1. Department of Earth Science and Engineering, Imperial College London, UK.
2. Fluid Dynamics and Solid Mechanics Group, Los Alamos National Laboratory, Los Alamos, New Mexico, USA.
3. Research School of Earth Sciences, Australian National University, Australian Capital Territory, Australia.
4. Lamont-Doherty Earth Observatory, Columbia University, New York, USA.
5. School of Earth and Ocean Sciences, University of Victoria, Victoria, British Columbia, Canada.
6. Department of Earth and Planetary Science, Harvard University, Massachusetts, USA.

*f.richards19@imperial.ac.uk

Estimates of global mean sea level during past warm periods provide an important constraint on ice sheet stability under prolonged warming and have been used to inform projections of future sea-level change. The Mid-Pliocene Warm Period (MPWP), ∼3 million years ago, has been a particular focus since it represents the most recent interval in Earth history with inferred temperatures and atmospheric CO_2 concentrations similar to those expected in the near future. Although several sea-level estimates for this period have been obtained from palaeoshoreline records, they differ by many metres due to spatially variable Pliocene-to-recent vertical motions of the crust, caused by geodynamic processes including sedimentary loading, tectonic activity, glacial isostatic adjustment, and mantle convection. To address this issue and place more robust bounds on the amplitude of MPWP sea level, we combine a continent-wide suite of Australian sea-level markers with geodynamic simulations to quantify and remove post-Pliocene vertical motions at the continental scale. We find that dynamic topography related to mantle convection is the dominant process responsible for deflecting Australian MPWP sea-level markers and that correcting for it and glacial isostatic adjustment yields a global mean sea-level estimate of $+16.0^{+5.5}_{-5.6}$ m ($50^{\text{th}}/16^{\text{th}}/84^{\text{th}}$ percentiles). Although this range is consistent with other estimates from geomorphic sea-level indicators, the upper bound is lower than assumed in recent ice sheet modelling studies, suggesting a significantly more stable Antarctic Ice Sheet under future warming scenarios.

Robust forecasts of future sea-level change are dependent on our ability to accurately model the response of ice sheets to climate change. As atmospheric temperatures and CO_2 concentrations continue to surpass those previously observed during human history, we must increasingly turn to the geological record of past warm periods to gain insights into ice-sheet sensitivity[1]. The Mid-Pliocene Warm Period (MPWP), approximately 3.3–3.0 million years ago (Ma), is of particular interest since global mean temperature was 1.9–3.6°C above pre-industrial levels and atmospheric CO_2 concentrations were $\sim$ 400 ppm, conditions comparable to those expected to prevail in the near future under many emissions scenarios[2,3,4,5]. Estimates of global mean sea level (GMSL) during this period have been used as a key constraint on future ice sheet stability in the face of prolonged warming[6,1].

An important problem with such an approach is that MPWP GMSL estimates exhibit significant variability between different studies. For example, ice-sheet modelling indicates that GMSL was 4–13 m above present day[7,8], but values of up to +26 m can be obtained if the poorly understood ice-sheet processes of meltwater-driven fracturing and ice cliff collapse (collectively known as the *marine ice-cliff instability*; MICI) are included[1]. Alternatively, attempts to constrain palaeo-ice volumes using temperature-corrected oxygen isotope records suffer from very large uncertainties[9], yielding MPWP GMSL estimates of +6–58 m[10,11,12].

The large uncertainties associated with these indirect constraints has led to renewed focus on the use of palaeoshoreline elevations and other geological markers of former sea level to more directly constrain MPWP GMSL[13,14,15]. Although these geomorphic estimates have, in many cases, been corrected for local uplift and subsidence, they span a range of +6–35 m (Table 1), indicating substantial and spatially variable vertical displacements of these features since their formation[16,17,18,15,19]. These displacements have been variably attributed to sediment redistribution, tectonic activity associated with earthquakes and faulting, glacial isostatic adjustment (GIA; i.e., sea-level variations caused by ice and ocean mass changes), or dynamic topography (i.e., vertical surface motions driven by mantle convection). Improving estimates of GMSL during the MPWP therefore requires the selection of field sites where sea-level markers are reliably dated and certain of these processes can be accurately quantified, while others can be reasonably assumed to have negligible impact. With these considerations in mind, we focus herein on Australian sea-level records.

The Australian record of Pliocene sea level

In many respects, Australia represents an ideal setting for estimating GMSL from geological markers. The continent is surrounded by passive margins and is relatively remote from major plate boundaries (except in the far north where it encroaches within $\sim$ 1000 km of the Java and New Britain Trenches). The most recent phase of continental rifting occurred between south Australia and Antarctica and had largely progressed to full seafloor spreading by Late Cretaceous times[20]. Internal deformation, as judged from the modern distribution of seismicity, Neogene fault scarps, and borehole-breakout data, indicates only modest strain rates[21]. Thus, tectonic deformation throughout the majority of the continent is minimal. Furthermore, away from the South Eastern Highlands and Flinders Ranges, Australia's topography is dominated by low elevation and low relief, resulting in slow rates of erosion and sediment redistribution in comparison to other major continents[22,23]. Australia's location in the far field of the former Laurentide and Fennoscandian ice sheets, in addition to Greenland and West Antarctica, means that the GIA-induced change in sea level from Pliocene to present day is dominated by a signal proportional to any difference in ice volumes across this period and a suite of more minor effects associated with remnant adjustment to the last glacial cycle[4]. The latter includes ocean syphoning, the flux of water toward and away from peripheral bulges surrounding locations of ancient ice cover as these bulges subside and uplift across glacial cycles, and continental levering, the shoreline-perpendicular tilting of the crust and mantle driven by ocean loading and unloading[24]. Of these effects, only levering introduces significant geographic variability in sea-level change across Australia, although this variability is less than ~ 5 m across coastal sites (Methods; Figure S8)[4,13,18].

In spite of these factors, Late Pliocene geomorphic indicators record local sea levels that vary by approximately ± 100 m around the continent (Figure 1a; Table 2). These constraints fall into two broad categories. Onshore, MPWP palaeoshoreline indicators are found in the Perth Basin (beach deposit at $\sim$40 m above sea level [m.a.s.l.])[25,26], Cape Range (marine terrace at 15–40 m.a.s.l.)[27], and the Roe Plain (marine terrace at 15–30 m.a.s.l.)[13]. The latter two have been dated to $\sim$2.7$\pm$0.3 Ma and $\sim$3.1$\pm$0.4 Ma, respectively, based on strontium isotope analysis of bivalve shells, while the former is interpreted to be of Late Pliocene age (2.6–3.6 Ma) based on biostratigraphic correlations. Offshore, relative sea-level (RSL) constraints include backstripped well data that record approximately -95 m of Pliocene-to-Recent water-loaded elevation change in the North Carnarvon Basin[28] and -180 m on the Marion Plateau[29] (see Table 2 and Methods for more details on each observation). Given the relative tectonic quiescence, slow rates of sediment redistribution, and minor GIA impacts, this raises the question: is dynamic topography responsible for this observed variability in Australian MPWP local sea-level estimates? If so, can we accurately account for this dynamic topographic deformation? And what GMSL estimate do we obtain if we make a correction for both dynamic topography and GIA?

Modelling Pliocene-to-Recent mantle flow

Invoking a significant role for dynamic topography in controlling Neogene vertical motions across Australia is not without precedent. Geological observations including the uplift and subsidence of paleoshorelines in the Eucla and Murray Basins, the width of continental shelves, stratigraphic geometries offshore, rapid subsidence of carbonate reefs on the Northwest Shelf, and volcanism and uplift of the Eastern Highlands as recorded by the fluvial geomorphological record, have all previously been attributed to the spatiotemporal evolution of mantle flow beneath the continent[34,29,28,35,36,37]. Nevertheless, before we can simulate the spatio-temporal evolution of Australian dynamic topography, we must first obtain models of the present-day mantle structure that are consistent with available geodynamic, seismic, and geodetic constraints.

We therefore adopt the approach of Richards *et al.*[32] to invert for mantle density models that simultaneously satisfy present-day estimates of dynamic topography, geoid height anomalies, core-mantle boundary excess ellipticity, Stoneley modes, and semi-diurnal body tides. These models include high-resolution upper mantle structure from surface wave tomography, account for anelastic effects and limited seismic resolution in the mid mantle, and incorporate dense basal layers within the large low velocity provinces (LLVPs). By varying the thickness and composition of the basal layer and predicting associated dynamic topography, geoid undulations, and CMB topography using instantaneous flow calculations, we obtain best-fitting density structures for 15 different combinations of radial viscosity profile (S10[38];F10V1[31]; F10V2[31]) and V_S tomographic model (LLNL-G3D-JPS[30]; S40RTS[39]; SAVANI[40]; SEMUCB-WM1[41]; TX2011[42]; Table S1). While the resulting geodynamic predictions provide good fit to observa-

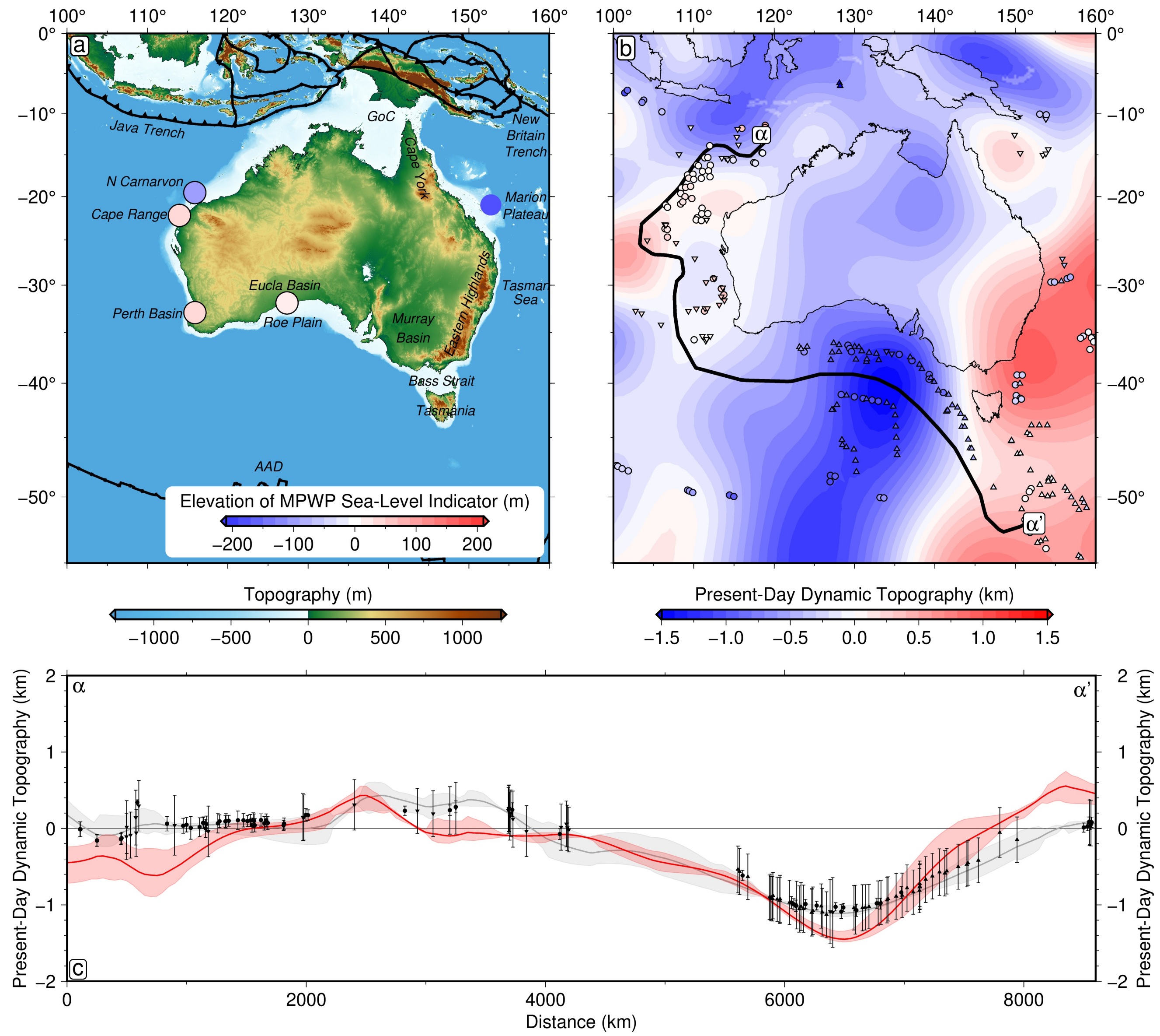

Figure 1: **Australian Pliocene sea-level markers and dynamic topography at the present day.** (a) Location map of study region. Circles = markers coloured by mean elevation of the palaeo sea-level indicator (see Table 2; GoC = Gulf of Carpentaria; N Carnarvon = North Carnarvon Basin; AAD = Australian-Antarctic Discordance. (b) Predicted present-day dynamic topography from instantaneous mantle flow calculation for density structure derived from LLNL-G3D-JPS tomographic model[30] and the F10V2 mantle viscosity profile[31], optimised to fit global constraints on dynamic topography, geoid undulations and CMB excess ellipticity[32]. Coloured circles/triangles = spot measurements of oceanic residual depth[33] (a common proxy for observed dynamic topography); thick black line = location of transect shown in panel (c). Predicted dynamic topography field is expanded up to spherical harmonic degree, $l_{max} = 30$. (c) Predicted versus observed present-day dynamic topography along NW-to-SE transect. Red line/band = prediction with uncertainties; circles/triangles with error bars = spot measurements of residual depth and uncertainties[33]; grey line/band = spherical harmonic fit to spot measurements ($l_{max} = 30$). Uncertainty bands represent range within 500 km-wide swath perpendicular to transect.

tional constraints at a global scale, agreement between predicted dynamic topography and oceanic residual depth measurements varies regionally. Critically, this agreement is particularly strong around the margins of Australia ($r = 0.76$–0.85 for all models; Figures 1b–c and S1; Table S1). This result confirms that our present-day mantle density models are likely robust beneath this region, thereby enabling us to hindcast mantle flow and associated changes in dynamic topography with some confidence.

To reconstruct the spatiotemporal evolution of Australian dynamic topography, we incorporate our suite of mantle density and viscosity models into numerical simulations of convection using the ASPECT software package[43,44]. In order to more fully explore uncertainties in our reconstructions, rather than using only the 15 optimised mantle density models, we generate a 270-model ensemble based on the same five seismic tomographic and three radial viscosity inputs, but with two different LLVP dense-layer vertical extents, five dense layer chemical density contrasts, and two plate motion histories (Methods). In all cases, free-slip boundary conditions are applied at the surface and core-mantle boundary (CMB), with plate reconstructions used to rotate output fields such that dynamic topography change is calculated in a Lagrangian reference frame.

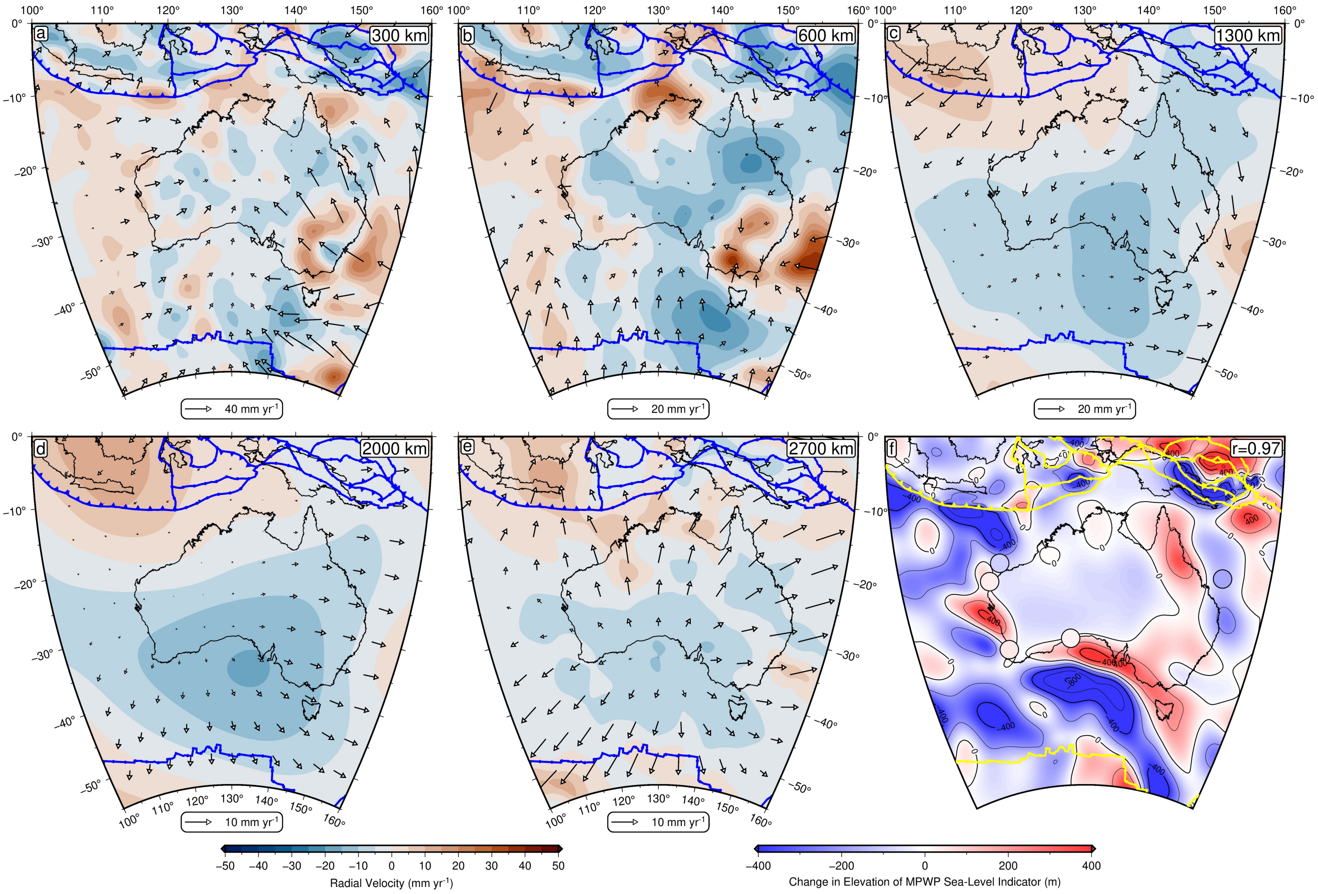

Figure 2: **Predicted pattern of present-day mantle flow beneath Australia and associated post-MPWP dynamic topography change.** (a) Radial component of mantle velocity at 300 km depth given by red-blue colourscale; arrows = tangential component; blue lines = plate boundaries. (b–e) Same as panel (a), except at 600 km, 1300 km, 2000 km and 2700 km depth, respectively. (f) Predicted change in elevation of Mid-Pliocene Warm Period sea-level marker due to dynamic topography evolution since 3 Ma. Circles = mid-Pliocene median uncorrected 3 Ma GMSL estimates (i.e., present-day elevation + palaeo-water depth; Table 2); yellow lines = plate boundaries. Convection simulation based on LLNL-G3D-JPS tomographic model[30] and F10V2 viscosity profile[31].

Despite this wide exploration of the parameter space, we nevertheless reconstruct consistent mantle flow patterns beneath Australia (representative examples are shown in Figures 2a–e, S3 and S4). In all cases, the long-wavelength pattern is dominated by cold anomalies sinking beneath a region stretching from the Australian-Antarctic Discordance in the southwest to the Coral Sea in the northeast, with deep mantle return flow northeastward towards the Pacific LLVP. Hot upwellings rooted in both the lower mantle and mid-mantle are predicted beneath Cape Range, Cape York, Tasmania, and the Eucla Basin. High-viscosity Australian lithosphere travels rapidly northeastwards over these flow structures, leading to strong shear-driven flow in the underlying asthenosphere[45]. This motion leads to rapid changes in dynamic topography within the reference frame of the Australian plate (~ 100 m Myr^{-1}), with substantial increases in dynamic topography predicted across Cape York and from Cape Range anti-clockwise around the coast into the Bass Strait (Figure 2f). Predicted amplitudes and spatial patterns vary moderately as a function of model input, but the distribution of uplift and subsidence is remarkably similar (Figures S5–S7). Most of these relative elevation change predictions are in strong agreement with palaeo sea-level observations (>50% yield a Pearson's correlation coefficient, r, between 0.73 and 0.97), lending confidence to our use of these dynamic topography simulations to correct post-depositional warping of palaeoshorelines on a continental scale. This inference is further strengthened by agreement of predicted vertical motions with indirect constraints on uplift and subsidence from seismic stratigraphy, river profile analysis, speleothem records, and the location of Neogene magmatism across the continent[46,34,29,35,36,37]. An important corollary is that it is essential to consider the impact of evolving dynamic topography on marker elevations in studies of former sea level[47,13,48].

Re-evaluating MPWP sea level

There are several important sources of uncertainty to consider when reconstructing GMSL using a suite of relative sea-level markers. First, the age of the marker, the palaeo-water depth in which it formed (i.e. its indicative range), and its present-day elevation are known to a limited degree of precision. Secondly, as previously discussed, Pliocene-to-Recent plate motion history, mantle density, and mantle viscosity are imperfectly constrained, feeding into appreciable uncertainty in corrections for dynamic topography and GIA. In regard to the latter, variations in elastic lithospheric thickness and upper mantle viscosity have the largest impact on the magnitude of predicted sea-level change due to their influence on continental levering (Figure S8). Finally, backstripped sedimentary records and coupled ocean-atmosphere–ice-sheet model simulations suggest that glacio-eustatic sea level variations may have occurred during the MPWP[18,49]. The exact amplitude and timing of these GMSL oscillations are, however, poorly constrained. Consequently, we have chosen to pose the determination of MPWP GMSL as a Gaussian process-based Bayesian inference problem, allowing these different sources of uncertainty to be robustly propagated into our final value. Within this framework, GMSL at time, t, is estimated from each sea-level marker at longitude, ϕ, and latitude, θ, according to

$$GMSL_{obs}(t) = e(\phi,\theta) + w_d - C_{GIA}(\phi,\theta,I,\eta,t) - C_{DT}(\phi,\theta,\rho,\eta,v,t), \quad (1)$$

where e is the present-day elevation, w_d is the paleo-water depth, C_{GIA} is the correction for GIA (see Methods for details of prediction), C_{DT} is the correction for dynamic topography, I is ice history, η is mantle viscosity, ρ is mantle density, and v is plate motion history. A Gaussian process composed of a radial basis function (RBF) and a white noise kernel is then used to interpolate in time between these corrected sea-level observations, providing a GMSL estimate that varies through time (Methods)[50]. Given the large uncertainties in the magnitude and pacing of MPWP glacio-eustatic cycles, instead of fixing parameters controlling the amplitude and wavelength characteristics of the time-dependent Gaussian process *a priori*, their most probable values are inferred directly from the input data. Posterior distributions for the different components of Equation (1) are then sampled using a Sequential Monte Carlo (SMC) algorithm.

Determining the uncertainty associated with the elevation, age, and palaeo-water depth of each sea-level marker is relatively straightforward and can be obtained from the associated field observations and laboratory analyses (Methods). However, doing the same for the the GIA correction and—more importantly in the case of Australia—the dynamic topography correction, requires knowledge of likely values of C_{GIA} and C_{DT} when I, v, ρ, and η are intermediate to the cases that we have already simulated. To avoid the computational expense of running thousands of additional simulations, we instead rapidly calculate their values using emulators (i.e., computationally efficient approximations of the full numerical simulations) by training two separate neural networks on synthetic data derived from the existing GIA and dynamic topography simulations (Methods). In both cases, 10% of the input data is excluded from the training process, allowing us to assess the ability of the networks to accurately predict GIA and dynamic topography fields for previously unseen input parameters. Once trained, these feed-forward networks can be incorporated into the SMC algorithm, allowing uncertainty associated with geodynamic processes to be characterised. This approach enables the model outputs that better explain spatial RSL variability to be effectively upweighted in a statistically robust manner, since they will naturally be sampled more frequently due to their superior likelihood.

The Bayesian inversion scheme yields a revised MPWP GMSL of $+16.0^{+5.5}_{-5.6}$ m (Figures 3c–e and S9–S12). By correcting for +1.2±0.6 m of thermosteric sea-level change (assuming a contribution of +0.2–0.6 m $°C^{-1}$ [51]), this range can be converted into an estimate of ice volume loss relative to the modern state, expressed as metres of global mean sea level equivalent (GMSLE). The resulting ~ 15 m median value suggests a considerable loss of ice from Greenland and West Antarctica, with the possibility of minor mass loss from East Antarctica. By contrast, the ~ 20 m upper bound would require significant additional loss of marine-based ice in East Antarctica[52]. The full +9.2–20.3 m GMSLE range is consistent with other recent estimates of MPWP ice loss, including +5.6–19.2 m GMSLE from speleothem overgrowths in the western Mediterranean[15], +5.0–15.5 m GMSLE from backstripped sea-level records in New Zealand (corrected assuming the same +1.2 m thermosteric contribution)[18], and +4–13 m GMSLE from ice-sheet models that exclude MICI processes[7,8]. It is, however, towards the lower end of most estimates that are based on analysis of oxygen isotopes in benthic foraminifera (e.g., +16.3–38.1 m GMSLE[10], +11.2–33.3 m GMSLE[12], and +11.1–31.2 m GMSLE[11]; all corrected with a +1.2 m thermosteric contribution).

Implications for predictions of future sea-level rise

Our MPWP GMSL estimate of $+16.0^{+5.5}_{-5.6}$ m is consistent with at least partial collapse of polar ice sheets and also has important ramifications for recent studies predicting future sea-level change. For example, the recent ice-sheet-model-based sea-level projections of De Conto *et al.*[1] are calibrated using an assumed MPWP sea-level contribution of 11–21 m from Antarctica alone. That study found that it is necessary to include both a marine ice-sheet instability (MISI) and strong MICI processes to obtain such substantial ice loss under MPWP climatic conditions. If Paris Agreement targets are exceeded, the authors showed that applying these same parameterisations of ice sheet behaviour to future melting scenarios leads to potentially rapid and irreversible sea-level rise.

After accounting for the smaller inferred extent of the mid-Pliocene Greenland ice sheet (thought to be a 5 ± 1 m

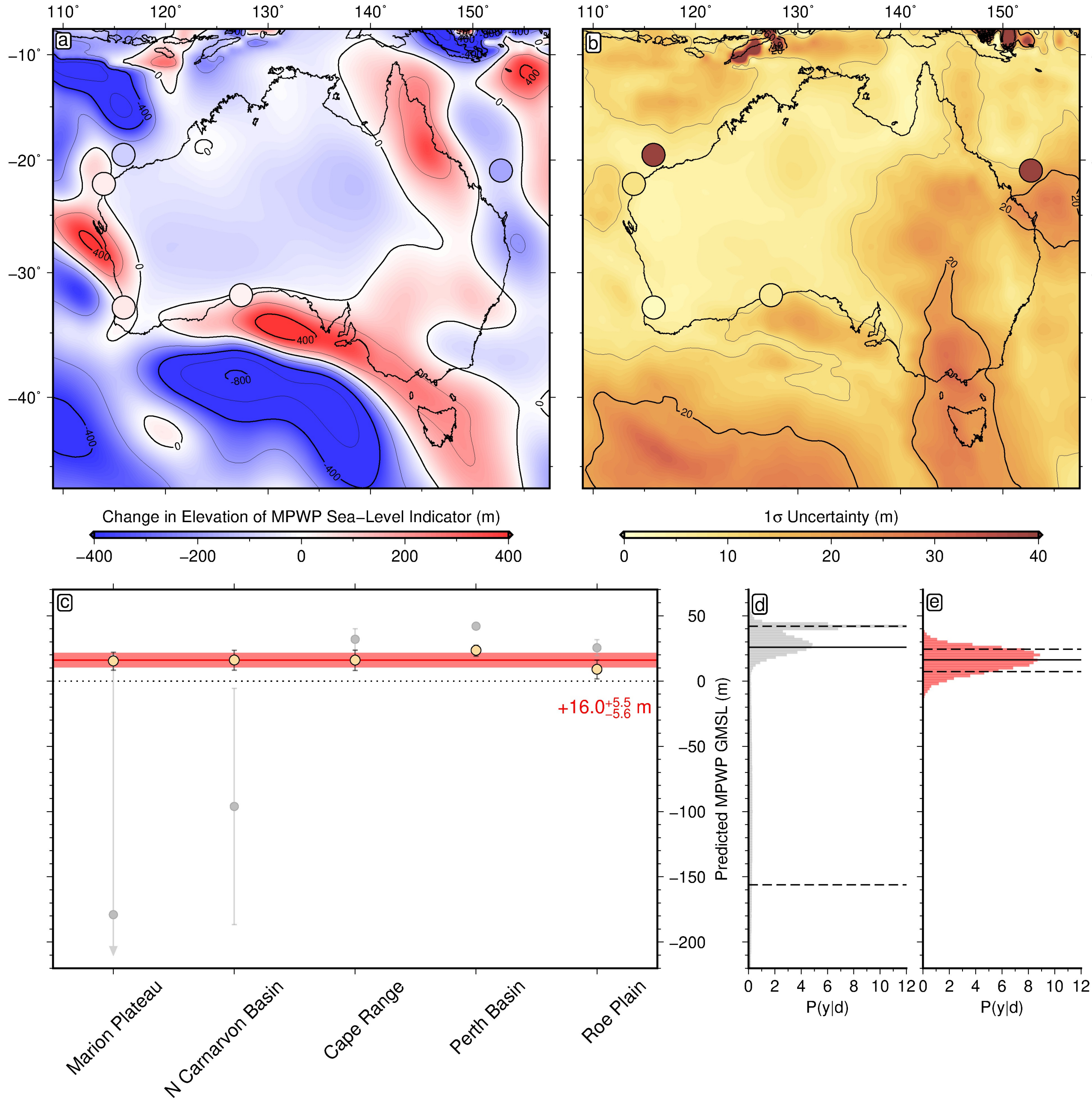

Figure 3: **Correcting MPWP relative sea-level markers for mantle dynamics.** (a) Median predicted change in MPWP sea-level marker elevation. Background colour = median of 3 Ma–Recent combined DT and GIA posterior probability distribution. Circles = mid-Pliocene median uncorrected 3 Ma GMSL estimates (i.e., present-day elevation + palaeo-water depth; Table 2). (b) Uncertainty on predicted elevation change. Background colour = 1σ uncertainty of 3 Ma–Recent combined DT and GIA posterior distribution. Circles = 1σ uncertainty of mid-Pliocene uncorrected 3 Ma GMSL estimates. (c) DT- and GIA-corrected 3 Ma GMSL along transect anti-clockwise from Cape Range. Yellow circles/error bars = $50^{th}/16^{th}$–84^{th} percentiles of DT- and GIA-corrected posterior distribution. Grey circles/error bars = same for uncorrected prior distribution. (d) Histogram of uncorrected 3 Ma GMSL prior distribution; solid/dashed lines = $50^{th}/16^{th}$–84^{th} GMSL percentiles. (e) Same for DT- and GIA-corrected 3 Ma GMSL.

GMSLE difference)[49] and a 1.2 ± 0.6 m thermosteric increase in mid-Pliocene sea level, our revised estimate for the Antarctic ice sheet contribution is $+9.8^{+5.6}_{-5.7}$ m GMSLE (total uncertainty calculated by propagating that of individual contributions under assumption they are mutually independent and uncorrelated). The upper end of this range overlaps the lower end of the De Conto *et al.* MPWP constraint of 11–21 m. Nevertheless, repeating their calibration process using our revised upper bound of $\leq +15.4$ m dramatically narrows the range of simulations that are consistent with observational targets (only 15 of their models pass versus the original 109). Restricting

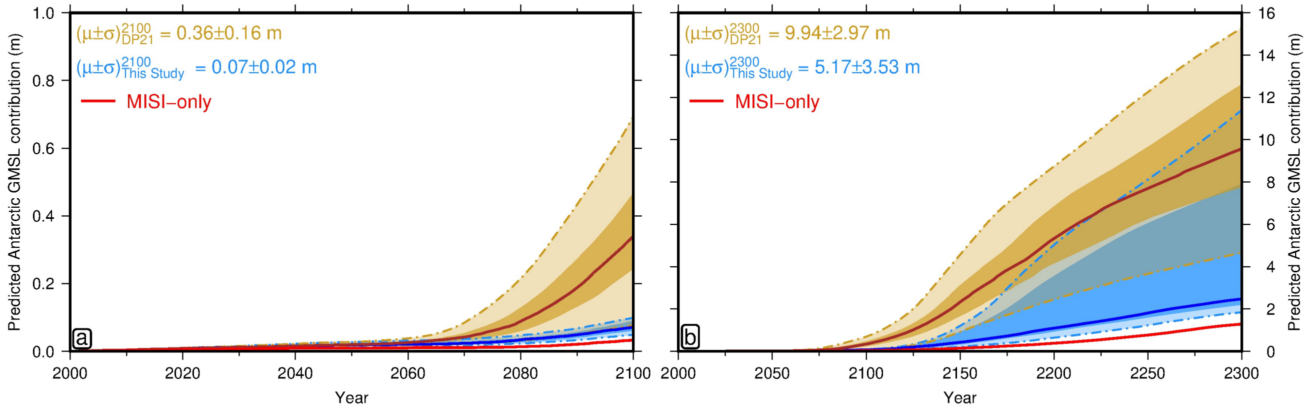

Figure 4: **Impact of revised MPWP GMSL estimate on future sea-level predictions.** (a) 2000-2100 Antarctic GMSL contributions under RCP8.5 (high-emissions scenario) based on simulations of De Conto *et al.*[1]. Yellow = projections consistent with their original +21±5 m MPWP GMSL value; blue = same for our revised value of $+16.0^{+5.5}_{-5.6}$ m; red = projections for ice-sheet models that exclude the MICI mechanism. Solid lines and dark/light shading = ensemble median and 50%/99% confidence intervals. (b) Same for 2000–2300 period.

ourselves to this reduced model ensemble leads to substantially slower and lower magnitude Antarctic contributions to future sea-level rise (i.e., the most extreme melting scenarios are excluded). Projected end-of-century GMSL rise under the RCP8.5 emissions scenario decrease by $\sim 70\%$ from $+34^{+21}_{-14}$ cm ($50^{th}/16^{th}/84^{th}$ percentiles), to $+7^{+2}_{-1}$ cm (Figure 4a). By 2300, the original and revised RCP8.5 ensemble projections become more comparable, but the median estimate (i.e., 50th percentile) remains $\sim 70\%$ smaller (approximately +2.5 m versus +9.6 m; Figure 4b).

Our revised end-of-century Antarctic sea-level predictions overlap with recent ensemble projections of ice-sheet models that do not incorporate the MICI mechanism ($+4^{+6}_{-5}$ cm for RCP8.5 [$50^{th}/16^{th}/84^{th}$ percentiles])[53]. In addition, our +16 m median MPWP GMSL estimate, which implies an Antarctic sea-level contribution of ∼10 m, also agrees well with mid-Pliocene ice sheet simulations that exclude MICI (e.g., 9.8 ± 2.1 m[54] and 7.8 ± 4.0 m[55]). Importantly, these results suggest that MICI processes need not be invoked to explain either MPWP ice volumes or to predict future Antarctic ice sheet contributions to sea-level change. Therefore, although the West Antarctic ice sheet may still be susceptible to runaway disintegration on multicentennial timescales, our work indicates that recent high-end projections envisaging a > 20 cm end-of-century Antarctic sea-level contribution under RCP8.5 and SSP5-85 emission scenarios are unlikely[1,53].

Methods

Compilation of relative sea-level constraints

All relative sea-level constraints used in this study have been compiled from pre-existing publications. The present-day elevations of Cape Range and Roe Plain MPWP sea-level markers have been accurately measured using Differential GPS (DGPS; ≤ 1 m uncertainty). In the case of the Roe Plain, the palaeoshoreline elevation is defined as 24 ± 6 m based on the spread of DGPS-derived scarp toe-line elevations sampled at Madura Quarry, Elarbilla, Carlabeencabba, and Boolaboola[13]. We restrict ourselves to using these DGPS-derived values since, unlike those inferred from digital elevation models, they have been groundtruthed via direct field survey and have significantly lower uncertainty. Similarly, at Cape Range, a palaeoshoreline elevation of 31 ± 8 m is derived from local averages of the three highest DGPS-sampled marine-limiting features on the Milyering Terrace and contacts between the Tulki Limestone and Exmouth Sandstone units[27]. In the Perth Basin, the mid-Pliocene palaeoshoreline is defined by the toe-line of the Whicher Scarp at 41 ± 1 m elevation, as inferred from Shuttle Radar Topography Mission data (30 m resolution)[26]. These estimates encompass along-scarp variations in elevation—we make no attempt to fit these local undulations since they are shorter wavelength than can be reliably resolved via our seismic tomography-based mantle flow models (< 200 km) and may instead represent unmodelled processes, such as neotectonics and sediment loading, which we treat as geological noise in our inversion scheme.

Offshore sea-level constraints are derived from backstripped well data. In each case, the local water-loaded elevation changes recorded by mid-Pliocene horizons are obtained by correcting for post-depositional sediment loading and compaction using the approach outlined in Kominz *et al.*[56] assuming Airy isostatic compensation. Since active rifting ceased between ∼70–160 million years ago at each well location, mid-Pliocene-to-Recent thermal subsidence is assumed to be negligible and no correction is made for this process. Data from the North Carnarvon Basin (-96 ± 91 m) is taken from Czarnota et al.[28], while the Marion Plateau constraint (-179 m ± 200 m) is derived from Di Caprio et al.[29] These offshore values include uncertainties arising from estimation of palaeo-water depths.

Table 1: Pre-existing geomorphic proxy-derived estimates of MPWP GMSL. * = 50$^{\mathrm{th}}$ (16$^{\mathrm{th}}$–84$^{\mathrm{th}}$ percentile); † = Virginia (US)/Wanganui (NZ)/ Enewetak (MH). Initials represent ISO3166 country codes.

Location	Estimated GMSL Range	Deposit Type	Reference	Uplift/Subsidence Correction
Orangeberg Scarp (US)	15–35 m	base of wave-cut scarp	[57,23]	+0–50 m uplift
Mallorca (ES)	17 (7 – 20) m*	speleothem overgrowth	[15]	∼-1 m GIA and 1–15 m uplift
De Hoop Plain (ZA)	22 – 31 m	base of wave cut scarp	[13,19]	no correction
Enewetak Atoll (MH)	20 – 25 m	buried coral reef horizon	[16]	112 – 115 m subsidence
Wanganui Basin (NZ)	11 (6 – 17) m*	backstripped sediments	[18]	no correction
Multiple Locations †	22 (17 – 27) m*	backstripped sediments	[58]	no correction

Numerical modelling of mantle convection

Our time-dependent mantle convection simulations employ the finite-element software, ASPECT (Advanced Solver for Problems in Earth's ConvecTion), which solves the coupled equations governing conservation of mass, momentum, and energy[43,59,44]. Solving these equations for time-evolving changes in temperature, velocity and pressure requires the specification of several boundary and initial conditions to produce a starting temperature, density and viscosity structure, as well as parameterisations for the rheological properties that govern their subsequent evolution.

Temperature Structure

In our simulations, the initial temperature field is determined using a hybrid approach. In the upper mantle, temperature anomalies above 400 km are derived from a modified version of the RHGW20 temperature and density model[60], which accounts for anelasticity at seismic frequencies and has been demonstrated to yield acceptable fits to present-day short-wavelength dynamic topography. Unlike RHGW20, which is based exclusively on the SL2013sv global surface wave tomographic model[61], the upper mantle model we adopt here is augmented with regional high-resolution tomographic studies in North America (SL2013NA[62]), Africa (AF2019[63]), and South America and the South Atlantic Ocean (SA2019[64]; see Hoggard *et al.*[65] and Richards *et al.*[32] for further details). Although, incorporating these high-resolution regional models does not affect inferred mantle structure beneath Australia, associated improvements in global dynamic topography and geoid predictions enhance the accuracy of calculated relative sea-level changes along the Australian margin. The lithosphere-asthenosphere boundary is delimited using the 1200 °C isothermal surface and we assume that temperature decreases linearly from this interface to the surface. Note that in the continental lithosphere, this thermal structure is adapted to produce neutral overall buoyancy (see following section).

Below 300 km, temperatures are derived from thermodynamic modelling. Following Austermann *et al.*[66], we assume a pyrolitic background mantle composition and use Perple_X alongside the thermodynamic database of Stixrude & Lithgow-Bertelloni[67] to generate a lookup table of anharmonic shear-wave velocities and densities, varying temperature from 300–4500 K in 50 K increments and pressure from 0–140 GPa in 0.1 GPa increments. At each depth, temperature-dependent discontinuities in density and seismic velocity caused by phase transitions are smoothed by adopting the median temperature derivative across a ±500°C swath either side of the geotherm[68]. Smoothed anharmonic velocities are then corrected for anelasticity using a Q profile determined using the approach of Matas & Bukowinski[69], as outlined in Richards *et al.*[32]. Having smoothed and corrected the V_S lookup table, velocities from five different seismic tomographic models—LLNL-G3D-JPS[30]; S40RTS[39]; SAVANI[40]; SEMUCB-WM1[41]; TX2011[42]—are converted into temperature, with values adjusted by a constant offset to ensure mean temperatures are consistent with the mantle geotherm[68]. Note that, following Richards *et al.*[32] and Davies *et al.*[70], we high-pass filter the seismic velocity models within the 1000–2000 km depth range in order to correct for vertical smearing of long-wavelength structure and obtain an acceptable fit to the observed long-wavelength geoid-to-topography ratio. This filtering is accomplished by multiplying the spherical harmonic coefficients, c_{lm}, of the seismic velocity fields with a monotonic truncation function, $f(l)$ that increases smoothly from 0 to 1 with spherical harmonic degree according to

$$f(l) = \begin{cases} -\left(\frac{l-l_{min}}{l_{max}-l_{min}}\right)^4 + 2\left(\frac{l-l_{min}}{l_{max}-l_{min}}\right)^2 & \text{for } l \leq l_{max} \\ 1 & \text{for } l > l_{max} \end{cases}$$

where $l_{min} = 1$ is the minimum spherical harmonic degree in the truncation (at which $f(l) = 0$) and $l_{max} = 8$ is the maximum degree (at which $f(l) = 1$). Between 300 km and 400 km depth, temperatures derived from the two parameterisations are smoothly merged by taking their weighted average.

Mapping temperature into density

To self-consistently convert these initial temperature fields into density distributions within ASPECT, we construct a radially averaged thermal expansivity profile that is compatible with both our upper and lower mantle V_S-to-density parameterisations (Figure S2). We also simplify our model calculations by assuming incompressible convection and therefore remove adiabatic increases in temperature and density with depth. Since heat flow measurements, xenolith geochemistry, seismic velocity, gravity, and topography observations suggest that compositional and thermal density contributions approximately balance each other within the continental lithosphere[71,72], we make these regions neutrally buoyant by resetting their temperature to the average of all external material at the relevant depth. Finally, following[32], we investigate the potential impact of chemical heterogeneity in the lowermost mantle by defining the bottom 0–200 km of LLVP regions as a separate compositional field with an excess density ranging from 0–132 kg m^{-3} (0–4% of the 3330 kg reference density, ρ_0).

Our mapping from temperature to density can therefore be expressed using

$$\rho(z, T, C) = \rho_0 \left[1 - \alpha(z)\left(T' - T_0\right)\right] + \Delta\rho_C C \tag{2}$$

where $\Delta\rho_C$ represents compositional excess density, C is the compositional field index ($C = 1$ inside the LLVP basal layer; $C = 0$ elsewhere). $\alpha(z)$ represents the radial thermal expansivity profile (Figure S2), $T_0 = 1600$ K is the reference temperature, and T' represents the temperature after subtraction of the adiabat ($T' = (T - T_{ad}) + T_0$). Note that in cases where either $\Delta\rho_C$ or basal layer thickness is equal to zero, C is set to zero throughout the model domain (i.e., these simulations are isochemical). In total, this approach generates 45 separate density models comprising different combinations of tomographically inferred initial temperature distribution, dense basal layer thickness, and compositional density anomaly.

Viscosity structure

Viscosity in each convection simulation is parameterised using three different radial profiles, $\eta_r(z)$, (S10[38], F10V1 and F10V2[31]), with lateral variations in viscosity incorporated using

$$\eta(z, T) = \eta_0(z)\epsilon_C C \exp\left[-\epsilon_T(z)\left(T - T_0\right)\right] \tag{3}$$

where $\epsilon_T(z)$ is the thermal viscosity exponent ($\epsilon_T(z) = 0.01$ for 0 km $\geq z \geq$ 670 km; $\epsilon_T(z) = 0.005$ for 670 km $> z \geq$ 2891 km), $\eta_0(z)$ represents the prescribed radial viscosity profile, and $\epsilon_C = 100$ represents the compositional viscosity exponent. The latter parameter applies to models in which the basal layers of LLVPs contain compositional anomalies ($C = 1$), since recent studies find that these regions likely contain smaller proportions of low-viscosity post-perovskite and larger volumes of high-viscosity silicic phases (e.g., stishovite and seifertite) compared to background mantle material[32]. This inference is further supported by recent work demonstrating that geoid observations are better matched by model predictions when LLVP material is assigned a similar viscosity to its surroundings, indicating that thermal and compositional controls on viscosity may counterbalance one another in the lowermost mantle[70].

Numerical model parameterisation

Equipped with these temperature, density, and viscosity inputs, we predict the time-dependent evolution of mantle circulation over the past 5 Myr using the backward advection method. This approach solves the governing equations in a forward sense, but with the sign of gravity reversed and thermal conductivity set to zero, since thermal diffusion is numerically unstable when reversed in time. The resulting absence of a diffusive term in the energy equation does progressively reduce numerical solution accuracy with each time step; however, this scheme has been shown to yield valid results over ≤ 30 Myr simulation periods[73] and considerably reduces computational expense relative to other 'retrodiction' methods, enabling a fuller exploration of density and viscosity uncertainties. Since ASPECT does not include self-gravitation, we impose the radially varying gravity profile from Glišović & Forte[74], while heat capacity is set to a constant value of 1250 J K^{-1} kg^{-1}. All simulations assume free-slip boundary conditions at both the surface and CMB. In the upper 1000 km of the mantle, our numerical grid has ~30 km radial resolution, increasing to ~ 90 km below this depth, while lateral resolutions in the same depth ranges are ~80 km and ~ 210 km, respectively. This resolution is achieved using an initial global mesh refinement of 4 and an adaptive refinement of 1 applied only to mesh points shallower than 1000 km depth.

Calculating relative sea-level change caused by dynamic topography

Using ASPECT, we calculate dynamic topography, h, at each time step of our simulation from the predicted normal stress, σ_{rr}, applied to the surface using

$$h = \frac{\sigma_{rr}}{(\mathbf{g} \cdot \mathbf{n})\, \Delta\rho} \tag{4}$$

where $(\mathbf{g} \cdot \mathbf{n})$ is the component of gravitational acceleration normal to the upper boundary and $\Delta\rho$ is the density difference between outer grid cells and the overlying material, assumed to be air in the ASPECT calculations (note that water loading in oceanic regions is accounted for in post-processing steps described below). To determine dynamic topography changes as a function of time at specific sites, it is important to account for plate motions over the intervening timespan. We do so by applying two different plate motion reconstructions—one based on GPS measurements[75]; the other on magnetic anomalies[76]—to translate the dynamic topography field calculated for each time period into its present-day coordinates before subtracting the rotated palaeo-dynamic topography field from its present-day equivalent. By calculating these outputs for each convection simulation and plate motion reconstruction, 270 separate dynamic topography histories are generated overall. To directly compare predicted dynamic topography changes to mid-Pliocene relative sea-level observations, we also account for changes in water loading caused by mantle dynamics. This correction adopts the framework described in Austermann & Mitrovica[77], which accounts for relative sea-level change arising from the predicted evolution of dynamic topography and associated geoid undulations at each time step.

Calculating relative sea-level change caused by glacial isostatic adjustment

GIA-induced changes in relative sea level since the mid-Pliocene Warm Period are calculated using the ice-age sea-level theory and pseudo-spectral algorithm (truncated at spherical harmonic degree and order 256) of Kendall *et al.*[78], as implemented in Raymo *et al.*[4]. The calculations require the Earth's depth-varying rheological structure to be specified in addition to an MPWP-to-Recent ice-loading history. We test two distinct ice-sheet loading histories. The first assumes that West Antarctica and Greenland were completely deglaciated before 2.95 Ma, while the East Antarctic Ice Sheet had an equivalent volume to the present-day ice sheet. After this time, the West Antarctic and Greenland ice sheets rapidly grow to present-day thicknesses. The second, by contrast, assumes a mid-Pliocene ice sheet configuration identical to the present day. After 2.95 Ma both reconstructions assume that ice volume varies according to scaled δ^{18}O from the LR04 benthic stack[79], with the corresponding geographic distributions based on ICE-5G model[80] time slices during periods with comparable δ^{18}O values. From the LIG to present day, ice volume simply varies according to the ICE-5G reconstruction. These two ice-sheet histories are paired with two different radial viscosity profiles to determine the spatially variable changes in relative sea level since the MPWP caused by GIA: VM2 (90 km elastic lithosphere, $\sim 5 \times 10^{20}$ Pa s upper mantle viscosity, and 2–3 $\times 10^{21}$ Pa s lower mantle viscosity); and LM (120 km elastic lithosphere, $\sim 5 \times 10^{20}$ Pa s upper mantle viscosity, and 5×10^{21} Pa s lower mantle viscosity).

Our GIA simulations based on these inputs incorporate time-varying shorelines owing to local flooding and regression, the growth and deglaciation of grounded marine-based ice sheets, the associated migration of water into or out of these marine settings, and the feedback between sea level and perturbations of Earth's rotation vector[78,81]. Note that we remove the eustatic global mean sea-level signal produced by each reconstruction (either 0 m or 14 m), since we aim to reconcile spatial variations in relative sea-level markers while making no prior assumption about palaeo-ice volume.

Constructing neural network emulators

To generate reasonable dynamic topography predictions for combinations of density, viscosity, and plate motion inputs that are intermediate to those of our 270 numerical simulations, we train a neural network using synthetic data drawn from these simulations. 10% of this input data is held back from the training process, allowing us to later validate the performance of the network on data it has not learned from. The remaining 90% is fed into a neural network with three fully connected dense layers containing 512 nodes with rectified linear unit activation functions. The final output layer has linear activation and produces a one-dimensional vector containing the dynamic topography prediction for a given input parameter set.

By comparing network predictions with target outputs for a known set of input parameters, backward propagation of errors is used to train the weights and biases in the network layers to improve performance. Input parameters for the model include indices for each tomographic model [0–1], indices for each viscosity profile [0–1], a plate motion index [0–1], LLVP dense layer thickness [0–200 km], chemical density difference [0–132 kg m^{-3}], age [2–4 Ma], latitude [7.368–46.667°S], and longitude [108.98–157.5°E]. To improve learning efficiency, we first normalise these inputs to have zero mean and a unity standard deviation. The network is subsequently optimised using an adaptive learning rate algorithm known as Adam[82]. Training was halted after 500 epochs, where training and validation loss reached ~ 1 m and showed no further improvement over a 20-epoch period. The set of learnt weights and biases associated with the minimum value of validation loss are then hard-coded into our Bayesian inverse modelling framework to rapidly simulate dynamic topography for any random sample of input parameters.

A similar approach is taken to emulate GIA predictions for models with viscosities and ice histories in-between the four end-member combinations used in our full numerical simulations. However, since the synthetic training dataset available in this case is smaller, we found it was necessary to modify our network structure to include 20% dropout layers between each of the three dense, fully connected layers. Training for this network is stopped after 100 epochs when validation loss ceased to improve beyond its minimum value of $\sim$0.5 m.

Bayesian inference of Mid-Pliocene GMSL

We evaluate GMSL during the MPWP using a Bayesian Gaussian process regression framework that integrates our MPWP relative sea-level constraints, and their associated age, elevation and water depth uncertainties, with the trained weights and biases of our dynamic topography and GIA neural network emulators. The principal advantage of this approach is that it enables uncertainties associated with both observations and predictions of post-depositional geodynamic processes to be propagated into our assessment of GMSL in a statistically robust manner.

It is assumed that GMSL variation as a function of time, $f(t)$, can be approximated by a Gaussian process comprising a radial basis function (RBF), and a mean function, $\mu(t)$, using the expression

$$f(t) \sim \mathcal{GP}\left[\mu_{GP}\left(t\right), k_{RBF}(t,t')\right]. \tag{5}$$

k_{RBF} is the RBF kernel, which takes two input points, t and t', and calculates a similarity measure between the two in the form of a scalar according to

$$k_{RBF}(t,t') = \sigma_{GP}^2 \exp\left(-\frac{\left\|(t-t')^2\right\|}{2\lambda_{GP}^2}\right), \tag{6}$$

where σ_{GP}^2 is the variance of the function and λ_{GP} is the timescale. The GMSL observations, $GMSL_{obs}(t)$ from Equation (1), are then assumed to represent the unknown function $f(t)$ plus random noise, ϵ of the form

$$\epsilon \sim \left|\mathcal{N}\left(0, \Sigma\right)\right|, \tag{7}$$

yielding the relationship between the Gaussian process and the observations

$$GMSL_{obs}(t) = f(t) + \epsilon. \tag{8}$$

Locality	Lat.	Lon.	Elev. (m)	Elev. 1σ (m)	PWD (m)	PWD 1σ (m)	Age (Ma)	Age 1σ (Ma)	Ref.
Cape Range	113.977	-22.179	31	8	1	1	2.69	0.29	27
Perth Basin	115.912	-32.926	41	1	1	1	3.10	0.50	26
Roe Plain	127.364	-31.903	24	6	2	2	3.05	0.35	13
Marion Pl.	152.733	-20.965	-179	2	0	200	3.30	0.45	29
N Carnarvon	115.893	-19.518	-96	13	0	90	3.05	0.30	28

Table 2: **MPWP sea-level localities.** Pl. = Plateau; Lat. = Latitude; Lon. = Longitude; Elev. = Elevation, PWD = palaeo-water depth; Ref. = Reference. Note that, for offshore markers, elevation uncertainty reflects compaction parameter uncertainties in backstripping procedure, while palaeo-water depth represents change between MPWP and present instead of absolute palaeo-water depth at time of deposition. This definition is equivalent in terms of corrected elevation, $e_c = e - w_d(t)$, to that used onshore since, within error, water depth has not changed since the MPWP in these locations (i.e., if present-day water depth were included in e and palaeo-water depth in $w_d(t)$, these terms would cancel out when evaluating e_c).

Instead of fixing their values, we set prior distributions for the Gaussian process parameters. The timescale prior (λ_{GP}) is an inverse Gaussian distribution with mean $\mu = 2$ kyr and shape parameter $\lambda = 5$ kyr, thereby encoding the assumption that any mid-Pliocene sea-level variability recorded in our constraints is on the typical interglacial timescale of a few kyrs. A normal distribution with $\mu = 0$ m and $\sigma = 1$ m is used as a prior for the square root of the variance (σ_{GP}), thereby allowing for modest MPWP GMSL variability on interglacial timescales without presupposing its presence. The mean (μ_{GP}) is assigned a Gaussian prior with $\mu = 20$ m and standard deviation $\sigma = 20$ m based on the range of pre-existing estimates of MPWP sea level from previous studies (Table 1). The noise (ϵ) prior is a half-normal distribution (i.e., positive values only) with $\mu = 0$ m and $\sigma = 2$ m. Age, water depth, and elevation uncertainties are assumed to be Gaussian, with means and standard deviations summarised in Table 2. Uniform priors were assumed for all emulator inputs, with an additional constraint in the case of the dynamic topography emulator that the sum of the five tomographic model indices and that of the three viscosity profile indices must both be equal to unity (i.e., total model contributions >100% are prohibited).

Posterior GMSL distributions are calculated using a Sequential Monte Carlo (SMC) algorithm implemented via the probabilistic programming package PyMC3[83], with likelihood of a given parameter sample determined based on cumulative misfit between the associated Gaussian process function and individual relative sea-level observations corrected for water depth, GIA, and dynamic topography (i.e., $GMSL_{obs}(t)$). This methodology is chosen for its ability to fully sample the potentially multimodal probability distributions we might expect for certain of the input parameters. To ensure sufficiently dense sampling, we compute six independent SMC chains, each with 2000 draws, and evaluate the resulting Gelman-Rubin and Effective Sample Size statistics to confirm the convergence of the algorithm. We further validated our approach via tests conducted on synthetic data generated from a prescribed GMSL function, randomly selected GIA and dynamic topography predictions, and the elevation, age, and water depth uncertainties of the relative sea-level observations. In these tests, the prescribed GMSL lies within the $\pm1\sigma$ region of the GMSL posterior derived from the synthetic observations, confirming the robustness of this approach.

Recalibration of sea-level projections

The impact of our revised $+16.0^{+5.5}_{-5.6}$ m mid-Pliocene GMSL estimate on recent projections of future Antarctic contributions to sea-level change is assessed by repeating the binary history matching procedure described in De

Conto *et al.*[1]. We focus on their RCP8.5 calculations since outputs are provided for the full, raw ensemble of input parameter values in this case ($n = 196$); whereas, for other emissions scenarios, the available ensembles have been trimmed using palaeo sea-level and satellite constraints ($n = 109$). The constraints they apply to calibrate their ice-sheet model ensembles include: i) observed ice mass loss between 1992 and 2017 from altimetry, gravimetry and input-output methods (i.e., Ice sheet Mass Balance Inter-Comparison Exercise (IMBIE)[84]; equivalent to 15–46 mm yr^{-1} GMSL change); ii) estimated Antarctic contributions to LIG GMSL (4.6 ± 1.5 m); and iii) estimated Antarctic contributions to mid-Pliocene GMSL (16 ± 5 m).

As in their analysis, we find that 163 models are consistent with the IMBIE constraint and 119 with both IMBIE and LIG target values. However, replacing their original mid-Pliocene GMSL estimate of 21 ± 5 m with our revised $+16.0^{+5.5}_{-5.6}$ m value dramatically reduces the number of models consistent with all three constraints (15 versus 109). This restricts the range of parameters controlling the MICI mechanism from 107 ± 54 m^{-1} yr^2 to 7 ± 7.5 m^{-1} yr^2 for the hydrofracturing prefactor, CALVLIQ, and 7.7 ± 3.3 km yr^{-1} to 8.6 ± 2.6 km yr^{-1} for the maximum calving rate parameter, VCLIFF. Consequently, although inclusion of both marine ice-sheet instability (MISI) and marine ice-cliff instability (MICI) mechanisms is required to fit the full range of revised constraints, the hydrofracturing component of MICI becomes a significantly smaller overall contributor.

References

[1] DeConto, R. M. *et al.* The paris climate agreement and future sea-level rise from antarctica. *Nature* **593**, 83–89 (2021).

[2] Haywood, A. M. *et al.* Large-scale features of pliocene climate: results from the pliocene model intercomparison project. *Climate of the Past* **9**, 191–209 (2013).

[3] De La Vega, E., Chalk, T. B., Wilson, P. A., Bysani, R. P. & Foster, G. L. Atmospheric co2 during the mid-piacenzian warm period and the m2 glaciation. *Scientific reports* **10**, 1–8 (2020).

[4] Raymo, M. E., Mitrovica, J. X., O'Leary, M. J., DeConto, R. M. & Hearty, P. J. Departures from eustasy in pliocene sea-level records. *Nature Geoscience* **4**, 328–332 (2011).

[5] Burke, K. D. *et al.* Pliocene and eocene provide best analogs for near-future climates. *Proceedings of the National Academy of Sciences* **115**, 13288–13293 (2018).

[6] DeConto, R. M. & Pollard, D. Contribution of antarctica to past and future sea-level rise. *Nature* **531**, 591–597 (2016).

[7] Pollard, D. & DeConto, R. M. Modelling west antarctic ice sheet growth and collapse through the past five million years. *Nature* **458**, 329–332 (2009).

[8] Koenig, S. *et al.* Ice sheet model dependency of the simulated greenland ice sheet in the mid-pliocene. *Climate of the Past* **11**, 369–381 (2015).

[9] Raymo, M. E., Kozdon, R., Evans, D., Lisiecki, L. & Ford, H. L. The accuracy of mid-pliocene δ18o-based ice volume and sea level reconstructions. *Earth-Science Reviews* **177**, 291–302 (2018).

[10] Dwyer, G. S. & Chandler, M. A. Mid-pliocene sea level and continental ice volume based on coupled benthic mg/ca palaeotemperatures and oxygen isotopes. *Philosophical Transactions of the Royal Society A: Mathematical, Physical and Engineering Sciences* **367**, 157–168 (2009).

[11] Rohling, E. *et al.* Sea-level and deep-sea-temperature variability over the past 5.3 million years. *Nature* **508**, 477–482 (2014).

[12] Miller, K. G. *et al.* Cenozoic sea-level and cryospheric evolution from deep-sea geochemical and continental margin records. *Science advances* **6**, eaaz1346 (2020).

[13] Rovere, A. *et al.* The mid-pliocene sea-level conundrum: Glacial isostasy, eustasy and dynamic topography. *Earth and Planetary Science Letters* **387**, 27–33 (2014).

[14] Horton, B. P. *et al.* Mapping sea-level change in time, space, and probability. *Annual Review of Environment and Resources* **43**, 481–521 (2018).

[15] Dumitru, O. A. *et al.* Constraints on global mean sea level during pliocene warmth. *Nature* **574**, 233–236 (2019).

[16] Wardlaw, B. R. & Quinn, T. M. The record of pliocene sea-level change at enewetak atoll. *Quaternary Science Reviews* **10**, 247–258 (1991).

[17] Rovere, A. *et al.* Mid-pliocene shorelines of the us atlantic coastal plain—an improved elevation database with comparison to earth model predictions. *Earth-Science Reviews* **145**, 117–131 (2015).

[18] Grant, G. *et al.* The amplitude and origin of sea-level variability during the pliocene epoch. *Nature* **574**, 237–241 (2019).

[19] Hearty, P. *et al.* Pliocene-pleistocene stratigraphy and sea-level estimates, republic of south africa with implications for a 400 ppmv co2 world. *Paleoceanography and paleoclimatology* **35**, e2019PA003835 (2020).

[20] Williams, S. E., Whittaker, J. M., Halpin, J. A. & Müller, R. D. Australian-antarctic breakup and seafloor spreading: Balancing geological and geophysical constraints. *Earth-Science Reviews* **188**, 41–58 (2019).

[21] Sandiford, M. Quaternary faulting record with seismicity and. *Evolution and dynamics of the Australian Plate* **372**, 107 (2003).

[22] Heimsath, A. M., Chappell, J. & Fifield, K. Eroding australia: rates and processes from bega valley to arnhem land. *Geological Society, London, Special Publications* **346**, 225–241 (2010).

[23] Moucha, R. & Ruetenik, G. A. Interplay between dynamic topography and flexure along the us atlantic passive margin: Insights from landscape evolution modeling. *Global and Planetary Change* **149**, 72–78 (2017).

[24] Mitrovica, J. & Milne, G. On the origin of late holocene sea-level highstands within equatorial ocean basins. *Quaternary Science Reviews* **21**, 2179–2190 (2002).

[25] Collins, L. B. & Baxter, J. L. Heavy mineral-bearing strandline deposits associated with high-energy beach environments, southern perth basin, western australia. *Journal of the Geological Society of Australia* **31**, 287–292 (1984).

[26] Gee, R. D. Landscape evolution and cenozoic sea-levels of the geographe bay hinterland, southwestern australia. *Journal of the Royal Society of Western Australia* 1–19 (2022).

[27] Sandstrom, M. R. *et al.* Age constraints on surface deformation recorded by fossil shorelines at cape range, western australia. *GSA Bulletin* (2020).

[28] Czarnota, K., Hoggard, M., White, N. & Winterbourne, J. Spatial and temporal patterns of cenozoic dynamic topography around australia. *Geochemistry, Geophysics, Geosystems* **14**, 634–658 (2013).

[29] DiCaprio, L., Müller, R. D. & Gurnis, M. A dynamic process for drowning carbonate reefs on the northeastern australian margin. *Geology* **38**, 11–14 (2010).

[30] Simmons, N., Myers, S., Johannesson, G., Matzel, E. & Grand, S. Evidence for long-lived subduction of an ancient tectonic plate beneath the southern Indian Ocean. *Geophysical Research Letters* **42**, 9270–9278 (2015).

[31] Forte, A. M. *et al.* Joint seismic–geodynamic-mineral physical modelling of African geodynamics: A reconciliation of deep-mantle convection with surface geophysical constraints. *Earth and Planetary Science Letters* **295**, 329–341 (2010).

[32] Richards, F., Hoggard, M. J., Ghelichkhan, S., Koelemeijer, P. & Lau, H. Geodynamic, geodetic, and seismic constraints favour deflated and dense-cored LLVPs. *EarthArXiv* X55601 (2021).

[33] Hoggard, M. J., Winterbourne, J., Czarnota, K. & White, N. Oceanic residual depth measurements, the plate cooling model, and global dynamic topography. *Journal of Geophysical Research: Solid Earth* **122**, 2328–2372 (2017).

[34] Sandiford, M. The tilting continent: a new constraint on the dynamic topographic field from australia. *Earth and Planetary Science Letters* **261**, 152–163 (2007).

[35] Czarnota, K., Roberts, G., White, N. & Fishwick, S. Spatial and temporal patterns of australian dynamic topography from river profile modeling. *Journal of Geophysical Research: Solid Earth* **119**, 1384–1424 (2014).

[36] Engel, J. *et al.* Using speleothems to constrain late cenozoic uplift rates in karst terranes. *Geology* **48**, 755–760 (2020).

[37] Ball, P., Czarnota, K., White, N., Klöcking, M. & Davies, D. Thermal structure of eastern australia's upper mantle and its relationship to cenozoic volcanic activity and dynamic topography. *Geochemistry, Geophysics, Geosystems* **22**, e2021GC009717 (2021).

[38] Steinberger, B., Werner, S. C. & Torsvik, T. H. Deep versus shallow origin of gravity anomalies, topography and volcanism on Earth, Venus and Mars. *Icarus* **207**, 564–577 (2010).

[39] Ritsema, J., Deuss, A., Van Heijst, H. J. & Woodhouse, J. H. S40RTS: A degree-40 shear-velocity model for the mantle from new Rayleigh wave dispersion, teleseismic traveltime and normal-mode splitting function measurements. *Geophysical Journal International* **184**, 1223–1236 (2011).

[40] Auer, L., Boschi, L., Becker, T., Nissen-Meyer, T. & Giardini, D. Savani: A variable resolution whole-mantle model of anisotropic shear velocity variations based on multiple data sets. *Journal of Geophysical Research: Solid Earth* **119**, 3006–3034 (2014).

[41] French, S. W. & Romanowicz, B. Broad plumes rooted at the base of the Earth's mantle beneath major hotspots. *Nature* **525**, 95–99 (2015).

[42] Grand, S. P. Mantle shear–wave tomography and the fate of subducted slabs. *Philosophical Transactions of the Royal Society of London. Series A: Mathematical, Physical and Engineering Sciences* **360**, 2475–2491 (2002).

[43] Kronbichler, M., Heister, T. & Bangerth, W. High accuracy mantle convection simulation through modern numerical methods. *Geophysical Journal International* **191**, 12–29 (2012). URL `http://dx.doi.org/10.1111/j.1365-246X.2012.05609.x`.

[44] Bangerth, W., Dannberg, J., Gassmöller, R. & Heister, T. Aspect v2.1.0 (2019). URL `https://doi.org/10.5281/zenodo.2653531`.

[45] Duvernay, T., Davies, D. R., Mathews, C. R., Gibson, A. H. & Kramer, S. C. Linking intraplate volcanism to lithospheric structure and asthenospheric flow. *Geochemistry, Geophysics, Geosystems* **22**, e2021GC009953 (2021).

[46] Dickinson, J. A., Wallace, M. W., Holdgate, G. R., Gallagher, S. J. & Thomas, L. Origin and timing of the miocene-pliocene unconformity in southeast australia. *Journal of Sedimentary Research* **72**, 288–303 (2002).

[47] Rowley, D. B. *et al.* Dynamic topography change of the eastern united states since 3 million years ago. *science* **340**, 1560–1563 (2013).

[48] Austermann, J., Mitrovica, J. X., Huybers, P. & Rovere, A. Detection of a dynamic topography signal in last interglacial sea-level records. *Science Advances* **3** (2017).

[49] de Boer, B., Haywood, A. M., Dolan, A. M., Hunter, S. J. & Prescott, C. L. The transient response of ice volume to orbital forcing during the warm late pliocene. *Geophysical Research Letters* **44**, 10–486 (2017).

[50] Dyer, B. *et al.* Sea-level trends across the bahamas constrain peak last interglacial ice melt. *Proceedings of the National Academy of Sciences* **118** (2021).

[51] Meehl, G. *et al.* 2007: Global climate projections. In Solomon, S. *et al.* (eds.) *Climate Change 2007: The Physical Science Basis. Contribution of Working Group I to the Fourth Assessment Report of the Intergovernmental Panel on Climate Change* (Cambridge University Press, Cambridge, UK and New York, NY, USA, 2007).

[52] Blackburn, T. *et al.* Ice retreat in wilkes basin of east antarctica during a warm interglacial. *Nature* **583**, 554–559 (2020).

[53] Edwards, T. L. *et al.* Projected land ice contributions to twenty-first-century sea level rise. *Nature* **593**, 74–82 (2021).

[54] de Boer, B. *et al.* Simulating the antarctic ice sheet in the late-pliocene warm period: Plismip-ant, an ice-sheet model intercomparison project. *The Cryosphere* **9**, 881–903 (2015).

[55] Dolan, A. M., De Boer, B., Bernales, J., Hill, D. J. & Haywood, A. M. High climate model dependency of pliocene antarctic ice-sheet predictions. *Nature communications* **9**, 1–12 (2018).

[56] Kominz, M. A. *et al.* Late cretaceous to miocene sea-level estimates from the new jersey and delaware coastal plain coreholes: An error analysis. *Basin Research* **20**, 211–226 (2008).

[57] Dowsett, H. J. & Cronin, T. M. High eustatic sea level during the middle pliocene: Evidence from the southeastern us atlantic coastal plain. *Geology* **18**, 435–438 (1990).

[58] Miller, K. G. *et al.* High tide of the warm pliocene: Implications of global sea level for antarctic deglaciation. *Geology* **40**, 407–410 (2012).

[59] Heister, T., Dannberg, J., Gassmöller, R. & Bangerth, W. High accuracy mantle convection simulation through modern numerical methods. II: Realistic models and problems. *Geophysical Journal International* **210**, 833–851 (2017). URL `https://doi.org/10.1093/gji/ggx195`.

[60] Richards, F. D., Hoggard, M. J., White, N. & Ghelichkhan, S. Quantifying the relationship between short-wavelength dynamic topography and thermomechanical structure of the upper mantle using calibrated parameterization of anelasticity. *Journal of Geophysical Research: Solid Earth* **125**, e2019JB019062 (2020).

[61] Schaeffer, A. & Lebedev, S. Global shear speed structure of the upper mantle and transition zone. *Geophysical Journal International* **194**, 417–449 (2013).

[62] Schaeffer, A. & Lebedev, S. Imaging the north american continent using waveform inversion of global and usarray data. *Earth and Planetary Science Letters* **402**, 26–41 (2014).

[63] Celli, N. L., Lebedev, S., Schaeffer, A. J. & Gaina, C. African cratonic lithosphere carved by mantle plumes. *Nature Communications* **11**, 1–10 (2020).

[64] Celli, N. L., Lebedev, S., Schaeffer, A. J., Ravenna, M. & Gaina, C. The upper mantle beneath the South Atlantic Ocean, South America and Africa from waveform tomography with massive data sets. *Geophysical Journal International* **221**, 178–204 (2020).

[65] Hoggard, M. J. *et al.* Global distribution of sediment-hosted metals controlled by craton edge stability. *Nature Geoscience* **13**, 504–510 (2020).

[66] Austermann, J., Hoggard, M. J., Latychev, K., Richards, F. D. & Mitrovica, J. X. The effect of lateral variations in Earth structure on Last Interglacial sea level. *Geophysical Journal International* **227**, 1938–1960 (2021).

[67] Stixrude, L. & Lithgow-Bertelloni, C. Thermodynamics of mantle minerals–II. Phase equilibria. *Geophysical Journal International* **184**, 1180–1213 (2011).

[68] Schuberth, B. S. A. & Bunge, H. P. Tomographic filtering of high-resolution mantle circulation models: Can seismic heterogeneity be explained by temperature alone? *Geochem. Geophys. Geosyst.* **10**, Q05W03 (2009).

[69] Matas, J. & Bukowinski, M. S. On the anelastic contribution to the temperature dependence of lower mantle seismic velocities. *Earth and Planetary Science Letters* **259**, 51–65 (2007).

[70] Davies, D. R., Ghelichkhan, S., Hoggard, M., Valentine, A. & Richards, F. D. Observations and models of dynamic topography: Current status and future directions. *EarthArXiv* X55W5T (2022).

[71] Jordan, T. H. Composition and development of the continental tectosphere. *Nature* **274**, 544–548 (1978).

[72] Shapiro, S. S., Hager, B. H. & Jordan, T. H. The continental tectosphere and Earth's long-wavelength gravity field. *Lithos* **48**, 135–152 (1999).

[73] Moucha, R. *et al.* Dynamic topography and long-term sea-level variations: There is no such thing as a stable continental platform. *Earth and Planetary Science Letters* **271**, 101–108 (2008).

[74] Glišović, P. & Forte, A. M. Importance of initial buoyancy field on evolution of mantle thermal structure: Implications of surface boundary conditions. *Geoscience Frontiers* **6**, 3–22 (2015).

[75] DeMets, C., Gordon, R. G. & Argus, D. F. Geologically current plate motions. *Geophysical journal international* **181**, 1–80 (2010).

[76] Seton, M. *et al.* Global continental and ocean basin reconstructions since 200 ma. *Earth-Science Reviews* **113**, 212–270 (2012).

[77] Austermann, J. & Mitrovica, J. Calculating gravitationally self-consistent sea level changes driven by dynamic topography. *Geophysical Journal International* **203**, 1909–1922 (2015).

[78] Kendall, R. A., Mitrovica, J. X. & Milne, G. A. On post-glacial sea level–ii. numerical formulation and comparative results on spherically symmetric models. *Geophysical Journal International* **161**, 679–706 (2005).

[79] Lisiecki, L. E. & Raymo, M. E. A pliocene-pleistocene stack of 57 globally distributed benthic δ18o records. *Paleoceanography* **20** (2005).

[80] Peltier, W. R. Global glacial isostasy and the surface of the ice-age earth: the ice-5g (vm2) model and grace. *Annu. Rev. Earth Planet. Sci.* **32**, 111–149 (2004).

[81] Mitrovica, J. X., Wahr, J., Matsuyama, I. & Paulson, A. The rotational stability of an ice-age earth. *Geophysical Journal International* **161**, 491–506 (2005).

[82] Kingma, D. P. & Ba, J. Adam: A method for stochastic optimization. *arXiv* 1412.6980 (2014).

[83] Salvatier, J., Wiecki, T. V. & Fonnesbeck, C. Probabilistic programming in python using pymc3. *PeerJ Computer Science* **2**, e55 (2016).

[84] Shepherd, A. *et al.* Mass balance of the antarctic ice sheet from 1992 to 2017. *Nature* **558**, 219–222 (2018).

Corresponding authors: Correspondence should be addressed to F. Richards (f.richards19@imperial.ac.uk).
Acknowledgments: We thank K. Czarnota, S. Stephenson, S. Goes and G. Roberts for their assistance and discussions. FR acknowledges support from the Schmidt Science Fellows program, in partnership with the Rhodes Trust, and the Imperial College Research Fellowship Scheme. SC is supported by a Los Alamos National Laboratory Director's Postdoctoral Fellowship. MH acknowledges support from Geoscience Australia and the Australian Research Council's Discovery Early Career Researcher Award DE220101519. JA acknowledges support from the Vetlesen Foundation. We thank the Computational Infrastructure for Geodynamics (geodynamics.org) which is funded by the National Science Foundation under award EAR-0949446 and EAR-1550901 for supporting the development of ASPECT and the Imperial College Research Computing Service (https://doi.org/10.14469/hpc/2232) for providing computational resources.
Author contributions: The study was conceived and designed by FR. FR compiled the database of relative sea-level markers. The paper was written by FR and MH, with guidance from all authors. FR and MH developed input temperature and density models for geodynamic modelling. FR, SC and JA contributed to the development of the mantle convection modelling and postprocessing codes. BD helped to develop the Bayesian inverse modelling framework. JXM carried out glacial isostatic adjustment calculations.
Competing interests: The authors declare no competing financial interests.
Data availability: All data, including digital versions of dynamic topography predictions, are available in the manuscript or the Supplementary Information.